Catalysis Science & Technology

Accepted Manuscript

ROYAL SOCIETY OF CHEMISTRY

www.rsc.org/catalysis

Journal Name

ARTICLE

Surface oxygen vacancies over Co_3O_4 mediated catalytic formaldehyde oxidation at room temperature

Received 00th January 20xx,
Accepted 00th January 20xx

DOI: 10.1039/x0xx00000x

www.rsc.org/

Zhong Wang[a,b], Wenzhong Wang[*,a], Ling Zhang[a], and Dong Jiang[a,b]

Three kinds of Co_3O_4 catalysts with different concentration of surface oxygen vacancies were successfully synthesized through a solvothermal and subsequent thermolysis method. Room temperature catalytic removal of formaldehyde, which is one of the major indoor air pollutants and seriously harmful to human health, is achieved by these Co_3O_4 catalysts. The existence of surface oxygen vacancies were confirmed by XPS, Raman spectra. The concentration of oxygen vacancies were obtained via TGA data, which could reach 1.83% (atom ratio) in this study. H_2-TPR and O_2-TPD results reveal the essential role of surface oxygen vacancies played in catalytic oxidation of formaldehyde, which are reflected by the improved mobility of oxygen and facile formation of reactive oxygen species (ROS). As a consequence, the catalytic activity shows a direct relationship with the concentration of surface oxygen vacancies. The Co_3O_4 nanobelts exhibited the best performance of formaldehyde oxidation due to larger specific surface area, higher low-temperature reducibility and abundant active surface oxygen species. The high catalytic activity and stability of this Co_3O_4 catalyst without the introduction of noble metals as co-catalyst shows a potential practical application for formaldehyde removal at room temperature. This study reveals the key importance of surface oxygen vacancies in the catalytic oxidation activity and complements the common viewpoint of Co^{3+} is the major activity species in the Co_3O_4-based systems, and provides a possibility for developing high performance catalysts through surface-modification.

1. Introduction

Formaldehyde (HCHO) is a typical and major indoor air pollutant and is well recognized to be seriously harmful to human health.[1] The effective removal of HCHO from indoor air has become an important subject in environmental science. Great efforts have been made to combat HCHO pollution, among which, room temperature catalytic oxidative decomposition is considered to be the most promising one because this process is environmentally friendly and energy saving.[2] Oxide-supported noble metal (Pt, Pd, Au, and Ag) catalysts, such as Pt/MnO_x-CeO_2[3], Pt/TiO_2[4], Pd/TiO_2[5], Au/CeO_2[6], Au/Co_3O_4[7], Pt/AlOOH[8], Pt/Al_2O_3[2], Au/FeO_x[9], Ag/HMO[10] *etc.* have been widely studied due to their high catalytic activity at room temperature. If noble metals were not introduced, however, these catalysts will exhibit lower catalytic activities and high temperature is generally required to activate the oxidation reactions.[11-13] The high cost of noble metals and the potential need for additional thermal energy limits the practical use of these catalysts, and consequently, provides a strong motivation to seek more economical and efficient way for catalytic HCHO removal.

As one of the commonly available and general spinel structured oxides, Co_3O_4 have received extensive attention of various fields, such as Li-O_2 batteries[14], magnetic materials[15], gas sensing[16], particularly, in the field of heterogeneous catalysis.[17-20] It is well established that Co_3O_4 nanocrystals are an ideal substitute for noble metals for CO oxidation at low temperature.[21, 22] Xie et al.[17] reported that Co_3O_4 nanorods, in which {110} facets are exposed primarily, could catalyze CO oxidation completely at a temperature as low as -77 °C and even exhibit high activity in the presence of water. Recently, Co_3O_4 nanocrystals have also been widely reported in catalytic oxidation of VOCs, such as CH_4[19], C_2H_4[23], C_3H_8[24], toluene[25] and formaldehyde[7, 26, 27]. However, these studies focused on structure-, dimension- and crystal facet-dependent activities, while the surface defect as one other important influence factor of catalyst activity, has rarely been studied.

It is well known that the catalytic oxidation of hydrocarbon over Co_3O_4 involves the participation of reactive oxygen species (ROS).[28-30] Therefore, it is reasonable to expect that the catalyst with high oxygen mobility and the facile formation of highly active electrophilic oxygen species (O^- or O_2^-) will lead to superior catalytic oxidation activity. It has been widely reported that oxygen can be facilely charged ($^{\cdot}O_2^-$, O_2^{2-}, or O_4^{2-}) by the localized electrons at the surface oxygen vacancies (Vo) through molecular oxygen activation channel.[31,

---

[a] State Key Laboratory of High Performance Ceramics and Superfine Microstructure, Shanghai Institute of Ceramics, Chinese Academy of Sciences, 1295 Dingxi Road, Shanghai 200050, People's Republic of China. Fax: +86-21-5241-3122, Email: wzwang@mail.sic.ac.cn

[b] University of Chinese Academy of Science, Beijing 100049, People's Republic of China.

Electronic Supplementary Information (ESI) available: [HRTEM images, N_2 adsorption-desorption isotherms, concentration changes of formaldehyde and CO_2, and FT IR spectra]. See DOI: 10.1039/x0xx00000x

[32] This charged state of oxygen is the critical step to generate ROS, which will play an important role in following catalytic oxidation reaction. On the other hand, as reported by Metiu and co-workers, oxygen vacancies exposed at the surface are strong Lewis basic sites.[33] Taking the Lewis acidity nature of formaldehyde (initial reactant) and formic acid (intermediate product) into consideration[34], a catalytic surface with higher Lewis basicity (surface oxygen vacancies) corresponds to a higher adsorption and catalytic activity for HCHO oxidation elimination.

Herein, three kinds of Co_3O_4 catalysts with different concentration of surface oxygen vacancies were synthesized through a solvothermal and subsequent thermolysis route. The origin of the surface oxygen vacancies come from the reducing ambient and thermal treatment during the synthesis procedures.[35] The formation of surface oxygen vacancies and their relative concentrations were characterized by XPS, Raman spectra and TGA data. These catalysts were employed in the catalytic oxidation of HCHO at room temperature, and their catalytic activity shows a direct correlation with the corresponding variation of surface oxygen vacancies concentrations. H_2-TPR and O_2-TPD results reveal the mechanism of surface oxygen vacancies mediated catalytic oxidation activity. This work will deepen our understanding of the effect of surface oxygen vacancies on the catalytic oxidation reaction and paves a way for developing high performance catalysts through surface-modification.

2. Experimental

2.1 Synthetic procedures

2.1.1 Synthesis of Co_3O_4 nanobelts

Co_3O_4 nanobelts was synthesized through a topochemical transformation route from $Co(CO_3)_{0.5}(OH)\cdot 0.11H_2O$ nanobelts due to their close structural matching according to previous literature.[36] In a typical synthesis, 10 mL of aqueous ammonia (30%) was first mixed with 25 mL of EG under stirring for 2 min to form a homogeneous solution. Then, 1.5 mL of aqueous sodium carbonate solution (1 mol/L) was added to the mixture and stirred for another 2 min. Afterwards, 5 mL of aqueous cobalt nitrate solution (1 mol/L) was added to the mixture, continue stirring for 20 min. The resulting homogeneous solution was transferred into a Teflon-lined stainless steel tank with a volume of 50 mL which was then heated at 170 °C for 17h. The autoclave was then cooled down to room temperature, precipitate was collected by centrifugation and rinsed with deionized water and absolute ethanol for three times. The products were then freeze-dried and calcined in a program-controlled furnace at 250 °C for 4 h.

2.1.2 Synthesis of Co_3O_4 nanoplates

Co_3O_4 nanoplates was obtained from $Co(OH)_2$ as precursor.[37] Briefly, 1.2 g of $Co(NO_3)_2\cdot 6H_2O$ was dissolved in a mixture of 5 mL ethanol and 5 mL deionized water. Then, 1 g of PVP was added and the solution was stirred for 30 min. Afterwards, 25 mL of NaOH (0.4 mol/L) aqueous solution was slowly added. The resulting suspension was transferred into a Teflon-lined stainless steel tank and heated at 120 °C for 10 h. The precipitate was collected by centrifugation and rinsed with deionized water and absolute ethanol for three times. The products were then freeze-dried and calcined in a program-controlled furnace at 250 °C for 4h.

2.1.3 Synthesis of Co_3O_4 nanosheets

Co_3O_4 nanosheets were obtained via converting the $(NH_4)Co_8(CO_3)_6(OH)_6\cdot 4H_2O$ precursor synthesized by a hydrothermal method.[14] First, 4 mmol of $Co(NO_3)_2\cdot 6H_2O$, 8 mmol of urea and 0.4 g of CTAB were dissolved in 40 mL deionized water under vigorously stirring until a transparent red solution formed. The resulting homogeneous solution was transferred into a Teflon-lined stainless steel tank with a volume of 50 mL which was then heated in an oven at 140 °C for 12h. The precipitate was collected by centrifuged and rinsed with de-ionized water and absolute ethanol for three times. The products were then freeze-dried and calcined in a program-controlled furnace at 250 °C for 4h.

Bulk Co_3O_4 was synthesized by precipitation method according to previous literature.[38]

2.2 Characterization

Powder X-ray diffraction (XRD) was measured to characterize the as-prepared catalyst with a Rigaku D/MAX 2250V diffractometer using monochromatized Cu Kα (λ=0.15418 nm) ray radiation source, operated at 40 kV tube voltage and 100 mA tube current. The scanning rate was 2°/min in the range of 2θ=20-80°. Surface area measurements were performed at 77K using a Micromeritics Tristar 3000 Brunauer-Emmett-Teller (BET) analyzer. The field emission scanning electron microscope (FE-SEM) images were acquired on a JEOL JSM-6700F filed emission scanning electron microscope. Transmission electron microscopy (TEM, JEOL JEM-2100F, accelerating voltage 200 kV) characterization was performed to evaluate the morphologies and microstructures of the catalysts. High-resolution transmission electron microscopy (HRTEM) images were obtained and analyzed using the Digital Micrograph software (Gatan Inc.). Reduction behavior of catalysts was examined by temperature-programmed reduction (H_2-TPR) under a pure H_2 flow (50 mL/min) at a heating rate of 10 °C/min, the amount of H_2 uptake during the reduction was measured by thermal conductivity detector of a gas chromatography instrument. The oxygen temperature programmed desorption (O_2-TPD) analysis was performed on a Micromeritics Chemosorb 2750 instrument. The procedures were as followed: (1) each sample was pretreated under a He flow (50 mL/min) at 300 °C for 40 min; (2) the sample was purged with 4% O_2/He gas flow for 1h at room temperature for O_2 adsorption; (3) the sample was heated to 850 °C at a heating rate of 10 °C /min under a pure He gas flow. The signal of O_2 desorption was measured by thermal conductivity detector. X-ray photoelectron spectroscopy (XPS) analysis was performed on an ESCALAB 250 instrument (Thermo Scientific Ltd.) to study the chemical states of the samples. The C 1s signal was used to correct the charge effects. IR spectra were recorded on a Burker Tensor 27 spectrometer. Room temperature Raman spectra were recorded on a confocal microprobe Jobin Yvon Lab Ram Infinity Raman system with a laser excitation of 532 nm. Fourier transform infrared (FTIR) spectra were recorded with a Nicolet iS10 FTIR spectrometer ex-situ in air. Thermogravimetric (TG) analysis was recorded on an NETZSCH STA 449C. Specimens were placed in Pt crucibles, and TG-DTA data were recorded during heating from room temperature to 700 °C under flowing air (100 mL/min). A heating rate of 10 °C/min was used for all experiments.

2.3 Evaluation of catalytic activity

The catalytic oxidation activity of the as-prepared samples (50 mg) for formaldehyde degradation (260 ppm) was tested in a gas-closed vitreous reactor (capacity 650 mL) with a double-walled jacket with water for temperature control. During the experiment, the reaction temperature was kept at 25 °C by circulating water. The relative humidity was controlled by evaporating certain amount of water injected in the reactor through heating after being purged by pure air. It could be controlled in the range of 20-98% at 25 °C. The activity of the catalysts on HCHO oxidation was estimated by the concentration change of HCHO before and after the oxidation process. HCHO concentration in the reactor was analyzed by phenol spectrophotometric method. 10 mL gas sample containing trace HCHO was absorbed by 15 mL phenol reagent solution (1×10^{-4} wt %) for 5 min. Then, 1.2 mL (1 wt %) ammonium ferric sulfate solution was added as the coloring reagent. After being shaken and waiting for 15 min in the dark, HCHO concentration was determined by measuring light absorbance at 630 nm with a spectrophotometer (Hitachi U-3010 UV-vis spectrophotometer). CO and CO_2 were monitored by GC analysis (GC 7900, Teccomp) equipped with a TDX-01, 80-100 mesh packed column followed by a methane conversion furnace and a flame ionization detector (FID).

3. Results and discussion

3.1 Morphological structure

The field-emission scanning electron microscope (FE-SEM) images of Co_3O_4 catalysts are exhibited in Fig. 1. As shown in Fig. 1 a1, the nanobelts have a regular morphology with the length of 200 nm and width of 40 nm. The enlarged image (Fig. 1 a2) demonstrated that the nanobelts were composed by nanoparticles with a size range of 14-17 nm. Fig. 1 b shows the typical feature of nanoplates, which present a hexagonal shape with side length of 180 nm and thickness of 17-19 nm. SEM image of the Co_3O_4 nanosheets is presented in Fig. 1 c1, the triangle nanosheets were composed by nanoparticles with a size varying from 24 to 28 nm (Fig. 1 c2).

Fig. 2 a1 shows the TEM images of Co_3O_4 nanobelts. The thermal conversion process results in porous structure and a uniform size distribution with average size of ~ 15 nm is demonstrated. The corresponding high-resolution TEM image (Fig. 2 a2) shows the d-spacing about 0.282 nm and 0.241 nm, which are in good agreement with the standard data of (220) and (113) interplanar spacings for spinel structured Co_3O_4. More HRTEM images of Co_3O_4 nanobelts are given in Fig. S1 (see in SI). The FFT spot patterns (Fig. 2 a3) can be indexed as (111), (113) and (220) crystal planes along the [110] zone axis. Fig. 2 b1 shows the TEM images of Co_3O_4 nanoplates. The morphology of the nanoplates is hexagonal platelet with thickness of about 20 nm. The HRTEM image (Fig. 2 b2) shows the $(\bar{2}20)$ and $(20\bar{2})$ crystal planes with 0.276 nm d-spacing and interfacial angle of 60°, which indicated that the surface of the nanoplates are {111} exposed. Its corresponding FFT image (Fig. 2 b3) shows an hexagon spot array, which can be indexed as [111] zone axis. TEM image of the Co_3O_4 nanosheets is showed in Fig. 2 c1, which present a triangle shape composed by nanoparticles with average size of about 30 nm. From the lattice resolved HRTEM image (Fig. 2 c2) and corresponding FFT spot pattern (Fig. 2 c3), it can be indexed as (111) and (220) crystal planes along the [112] zone axis.

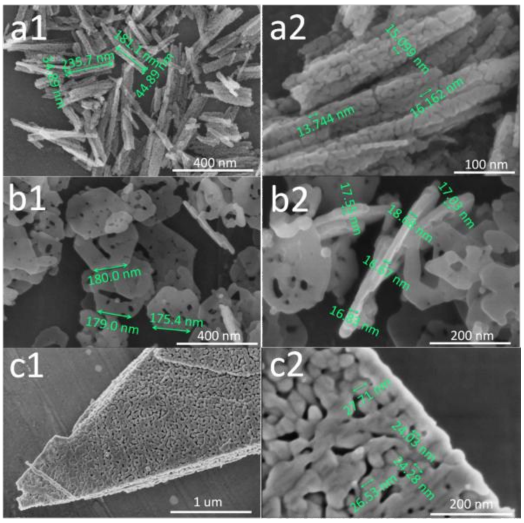

Figure 1. FESEM images of Co3O4 nanobelts (a1-a2), nanoplates (b1-b2) and nanosheets (c1-c2).

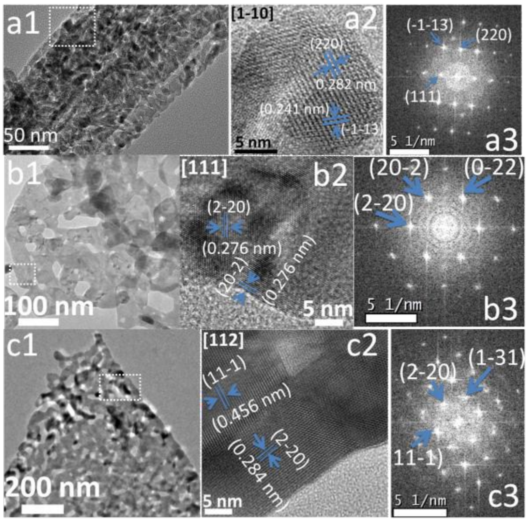

Figure 2. TEM, HRTEM, and fast-Fourier-transform (FFT) images of Co_3O_4 nanobelts (a1-a3), nanoplates (b1-b3) and nanosheets (c1-c3).

3.2 Textural characterization of catalysts

N_2 adsorption-desorption isotherms of different Co_3O_4 catalysts and their corresponding pore size distribution are shown in Fig. S2. All the samples show a typical H3 type loop, which indicate the aggregation of Co_3O_4 nanoparticles, revealing the slit-shaped pores of these catalysts. Their corresponding pore size distributions curves show that the pore sizes of Co_3O_4 catalysts are dominantly distributed between 2.0 nm and 6.0 nm. BET surface areas of the Co_3O_4 catalysts are listed in Table 1.

To further study the phase structure of Co_3O_4 catalysts, XRD measurements were carried out. Fig. 3a shows the XRD patterns of as-prepared Co_3O_4 samples. The peaks at 2θ of 31.3°, 36.8°, 44.8°, 59.5°, 65.2° correspond to the (220), (311), (400), (511), and (440) planes. All the diffraction peaks match well with the characteristic structure of the spinel Co_3O_4 (JCPDS No. 65-3103) without any impurity phase. The average particle sizes of all the samples calculated from the XRD data (FMWH of (311) peak) using the Scherrer equation are shown in Table 1. All these samples exhibit an average particle size between 15 to 25 nm, in good accordance with the observation from the SEM and TEM images. Compared with Co_3O_4 nanosheets, the diffraction peaks of Co_3O_4 nanoplates and nanobelts show an obvious shift to higher degrees (Fig. 3b), which can be ascribed to the presence of a structural disorder in the nanoplates and nanobelts.[39] The structural defects are supposed to larger the Co-O bond length and favorable for the formation of oxygen vacancies, which will make the extraction of O easier from the surface of Co_3O_4.[21] As indicated above, these catalysts with high oxygen mobility will significantly promote the catalytic oxidation activity.

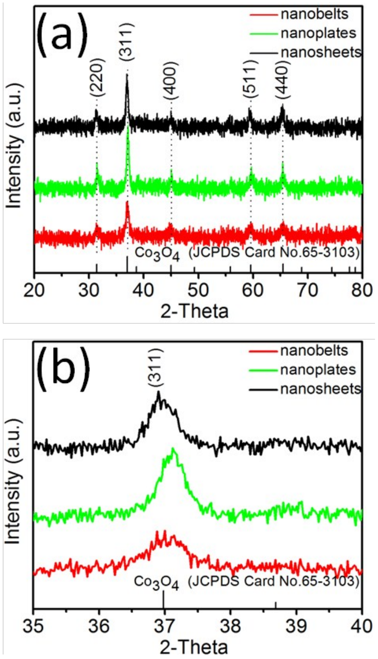

Figure 3. (a) XRD patterns of Co_3O_4 nanosheet, nanoplates and nanobelts. (b) Magnified peaks in 2θ range from 35 to 40°.

3.3 XPS spectra

X-ray photoelectron spectroscopy (XPS) was employed to gain further insight into the compositions and chemical states on the surface of the synthesized Co_3O_4 catalysts. The typical patterns of Co 2p and O 1s are presented in Fig. 4. According to the literature[26], the curve of Co 2p spectra were fitted into four peaks at binding energies of ~779.5, ~781.2, ~794.6 and ~797.1 eV, which are corresponding to Co^{3+} $2p_{3/2}$, Co^{2+} $2p_{3/2}$, Co^{3+} $2p_{1/2}$ and Co^{2+} $2p_{1/2}$ respectively.(Fig. 4a) The energy difference between the Co $2p_{3/2}$ peak and the Co $2p_{1/2}$ peak is ~15 eV, consistent with previous reports.[21, 40] The ration of Co^{3+}/Co^{2+} can be calculated from the XPS results as shown in Table 1. The small difference of Co^{3+}/Co^{2+} ration among these three samples are conform to the H_2-TPR test results as discussed below.

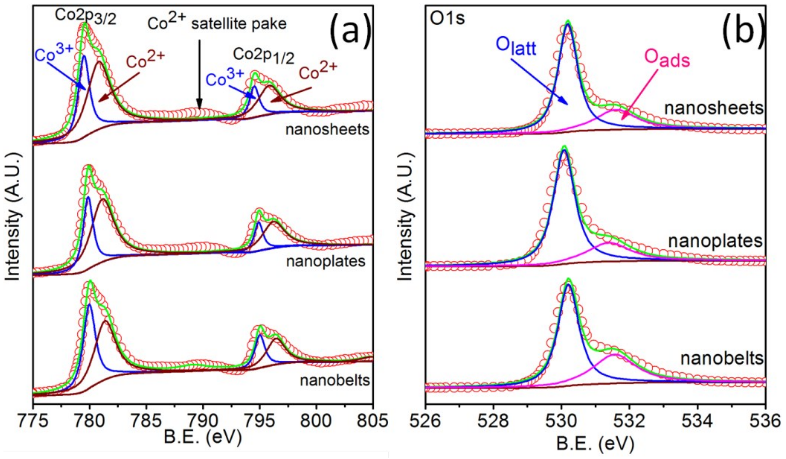

Figure 4. XPS spectra of the Co 2p (a) and O 1s (b) for various Co_3O_4 catalysts.

Table 1. Textural characteristic and surface composition of different Co_3O_4 samples.

Catalyst	BET surface area (m^2/g)	Particle size (XRD) (nm)	Co^{3+}/Co^{2+} (XPS)	k/S_{BET} ($min^{-1}*m^{-2}*g$)	O_{ads}/O_{latt} (XPS)	C/Co (XPS)	Concentration of Oxygen Vacancies (atom %)
nanobelts	61	17	40.3/59.7	1	36.2/63.8	0.205	1.93
nanoplates	21	21	33.7/66.3	0.145	27.3/72.7	0.137	1.02
nanosheets	39	25	36.1/63.9	-	24.6/75.4	0.149	0.14

3.4 Catalyst activity

The catalytic activities of different Co_3O_4 catalysts towards HCHO oxidation at room temperature are presented in Fig. 5. Each sample was measured for five cycles. Error bars in Fig. 5 (a) shown less than 10% difference with each cycle, which reflects the statistical reproducibility and stability for all the samples. As can be seen from the diagram, among the nanosheets, nanoplates and nanobelts, the nanobelts showed the highest catalytic activity for HCHO oxidation, which can completely eliminate 260 ppm formaldehyde in 30 minutes. This eliminate efficiency was comparable to, or even higher than, some oxide-supported noble metal catalysts.[41-43] The nanoplates showed less active while stable catalytic performance, which can oxidize 100 ppm formaldehyde in 60 minutes. The initial decrease in the nanosheets can be ascribed to adsorption because its content showed no change in the later detections. To verify the catalytic oxidation rather than adsorption had happened on Co_3O_4 nanobelts, the sealed reactor was heated to 80 °C for 15 min immediately after HCHO removal experiment, and then the concentration of HCHO in gas phase was monitored, which showed no detectable HCHO. FTIR experiments were performed to investigate the surface adsorbed species before and after the oxidation reaction (Fig. S3). For the original catalyst, the bands at 1385 cm-1 and 1520 cm-1 are attributed to surface adsorbed nitrate species and carbonate species, respectively, which are originated from the reactants of cobalt nitrate and sodium carbonate.[44] After reaction, no band located at 2845 cm^{-1}, which ascribed to the CH_2 asymmetric stretch of formaldehyde, was detected.[7] It has been reported that formate and dioxymethylene species on the surface of catalyst are critical by-products during HCHO oxidation.[26, 45] However, neither the bands at 1570 cm^{-1} and 1359 cm^{-1} attributed to $v_{as}(COO)$ and $v_s(COO)$ for the adsorbed formate species[46], nor the peaks at 2710 cm^{-1} and 2810 cm^{-1} belonging to the asymmetric and symmetric CH stretch of dioxymethylene[26], were detected. The big difference is the appearance of a band located at ~1630 cm^{-1}, which can be ascribed to bicarbonate species due to the adsorption of CO_2 and H_2O on the catalyst surface.[21] The change of CO_2 concentration during the reaction process were measured, which presented a fluctuant increase due to the CO_2 generating-adsorption process (Fig. S3), showed a good accordance with the FTIR results. This result confirms the occurrence of catalytic oxidation, rather than adsorption, of formaldehyde on our Co_3O_4 catalysts. However, the selectivity of converting HCHO to CO_2 was hard to be determined in this study due to the strong interaction between CO_2 and the catalyst surface.

In order to investigate the reusability of Co_3O_4 nanobelts catalyst in HCHO catalytic oxidation, the recycle performance was checked under the same conditions as mentioned above. After 20 cycles, the catalyst maintained 67% of its initial activity (eliminate 174 ppm HCHO in 30 min). The gradual deactivation can be ascribed to the accumulation of bicarbonate species on catalyst surface during the reaction as confirmed by the FTIR study, which inhibit the adsorption and activation of HCHO and O_2. The used catalyst was then regenerated at 120 °C under vacuum for 4h to remove the surface absorbed bicarbonate species (Fig. S3). The regenerated catalyst can recover to 86% of its initial activity (eliminate 223 ppm HCHO in 30 min), indicated the stable activity and high reproducibility of this Co_3O_4 catalyst.

Water vapor, the existence of which is unavoidable in ambient environment, has been known to play great influence on low-temperature catalytic oxidation reactions.[47] In order to investigate this factor, HCHO removal over Co_3O_4 nanoplates and nanobelts at room temperature with five relative humidity (RH) levels were carried out, as shown in Fig. 5d-4e. It is obvious that the HCHO removal efficiency was improved with the increase of RH up to 80% for nanobelts and up to 60% for nanoplates, respectively. Further increase of RH will somewhat inhibit the catalytic activity. These results suggest that water plays dual-character in determining the performance of Co_3O_4 catalysts. At low RH, the improved oxidation efficiency can be ascribed to the formation of hydroxyl groups dissociated from water on the surface oxygen vacancies sites, which favors the adsorption and transfer of oxygen[48] and benefits both the formation and the consumption of reaction intermediates[44]. Previous study even found that surface –OH could oxidize HCHO into formate and CO_2 in the absence of atmospheric oxygen.[49] When the RH beyond some critical concentration, water vapor will leads to severe catalytic deactivation due to its strong adsorption on the active sites, hindering O_2 and HCHO adsorption.[44]

The reaction rate constant (k) of nanoplates (Fig. 5b) and nanobelts (Fig. 5c) were calculated using pseudo-first-order kinetic model and the degree of fitting (R^2) reached more than 0.98, which indicated that the pseudo-first-order kinetic model could predict the reaction kinetics accurately. The reaction rate constant (k) of nanobelts is 20 times that of nanoplates, which are 0.14 min^{-1} and 0.0071 min^{-1} respectively. To avoid the inconformity effect caused by the difference of specific surface area, reaction rate constant of different Co_3O_4 samples were normalized by their BET surface area respectively, and the results are shown in Table 1. The normalized reaction rate constant of nanobelts is still 7 times that of nanoplates

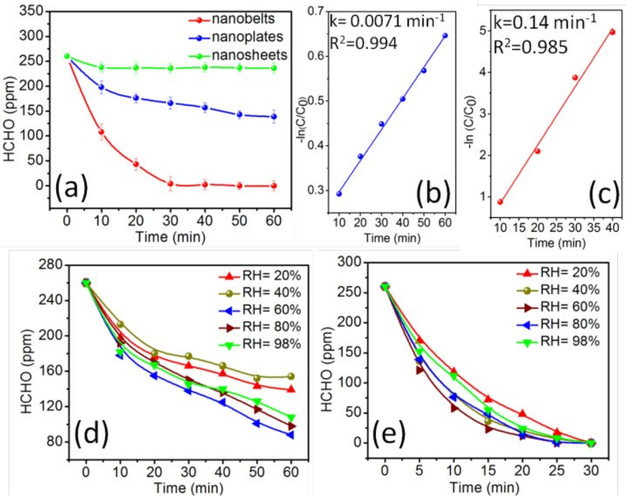

Figure 5. Catalytic activities. (a) Formaldehyde concentration changes as a function of reaction time for the different Co_3O_4 catalysts (RH= 20%). The error bars represent the maximum and minimum values and the dot indicate the average value from five experimental cycles. (b)-(c) Linear estimation of apparent rate constants (k) of Co_3O_4 nanoplates and nanobelts in panel (a) using the pseudo-first-order reaction kinetics. (d)-(e) The effect of relative humidity on formaldehyde removal efficiency over Co_3O_4 nanoplates and nanobelts.

It should be noted that, the Co_3O_4 catalysts here show no direct relationship with neither the Co^{3+} content nor the BET surface area (see Table 1), in contrast with previous reports[17, 27, 50] where Co^{3+} was generally treated as the mainly active species. Recent studies suggested that the surface oxygen vacancies could dramatically enhance the electrocatalytic performance of Co_3O_4 through delocalize the electrons around the Co-O bands.[51] Theoretical simulation also presented that the surface oxygen vacancies may provide a unique way for enhancing the catalytic activity of rutile MnO_2.[52] Moreover, oxygen vacancies (OVs) on the surface of BiOCl were found that prefer to activate oxygen into O_2^- or O_2^{2-}, depending on the location of OVs, which can promote the catalytic oxidation reactions significantly.[53] Additionally, Song *et al*. reported that the TiO_2 with surface oxygen vacancies could catalytic oxidize formaldehyde at room temperature without light.[54] Therefore, based on the above results and owing to the reducing ambient during the catalysts synthesis procedures, it is reasonable to expect that the catalytic performance of formaldehyde oxidation over Co_3O_4 catalysts could be surface oxygen vacancies mediated. Then, the existences of surface oxygen vacancies were characterized by Raman spectra and O1s XPS and their concentrations were calculated from the TGA data. The relationship between the concentrations of surface oxygen vacancies and the catalytic formaldehyde oxidation activity were fully discussed. And the results of H_2-TPR and O_2-TPD revealed that the mobility of oxygen and the ability of low-temperature oxygen activation were improved greatly by the surface oxygen vacancies, which are crucial factors for improving the catalytic activity.

3.5 Surface oxygen vacancies characterization

Fig. 4b shows the O 1s spectrum and its two fitted Gaussian peaks. The peak at ~530.2 eV corresponds to lattice oxygen species (O_{latt}), while the one located at ~531.8 eV can be ascribed to surface adsorption oxygen (O_{ads}).[55] The rations of O_{ads}/O_{latt} of different catalysts were shown in Table 1. The ration can be a yardstick to measure the amount of surface vacant oxygen, thus higher ration indicates larger surface oxygen vacancies. Therefore, the order of surface oxygen vacancies concentration is nanobelts > nanoplates > nanoshees. The relative concentration of surface oxygen vacancies shows a good consistence with the catalytic activity mentioned above.

The existence of surface oxygen vacancies are further confirmed by the Raman spectra. As reported, Raman bands at ~225, 480, 520, 683 cm^{-1} correspond respectively to the F1 2g, E_g, F2 2g, and A_{1g} modes of the pure Co_3O_4.[39] Among them, the band at ~225 cm^{-1} and 683 cm^{-1} can be ascribed to Raman vibration of Co^{2+}-O^{2-} and Co^{3+}-O^{2-} respectively.[21] As shown in Fig. 6, the Raman bands of the nanosheets fit very well with the standard pure Co_3O_4, indicated that the Co_3O_4 nanosheets have negligible structure disorders. Compared with the nanosheets, the Raman bands of the nanoplates and the nanobelts show an obvious shift to higher frequencies. The blue-shift of the Raman bands can be ascribed to the surface oxygen vacancies due to its photon-confinement effects.[56, 57] It should noted here that the overall enhancement of peak intensity in nanoplates sample probably due to the influence of crystallinity and the orientation effect during Raman test.

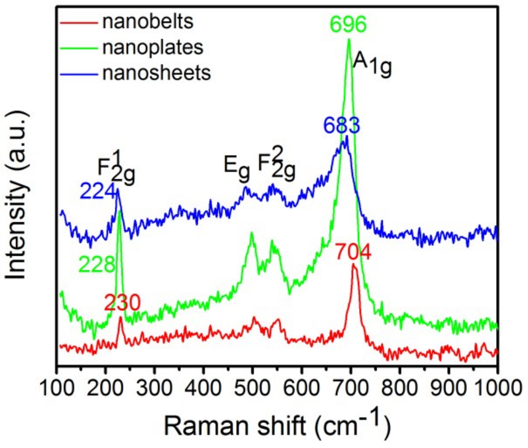

Figure 6. Raman spectra of Co_3O_4 nanosheets, nanoplates and nanobelts.

In order to further investigate the exact concentration of oxygen vacancies in nanobelts and nanoplates, the TGA curves in flowing air gas were measured. As shown in Fig. 7(a), bulk Co_3O_4 and Co_3O_4 nanosheets showed two weight loss stages in the temperature range of 40-700 °C. According to the literatures[58], the first weight loss can be ascribed to the loss of physical adsorption water molecules on the Co_3O_4 surface, while the second one can be assigned to the loss of chemisorption waters and the release of oxygen atoms on the surface of Co_3O_4 under high temperature. Compared with the bulk Co_3O_4, TGA curves of the nanoplates and nanobelts presented a similar trend of weight loss in the temperature range of 40-200 °C, but a more gentle weight loss in 200-400 °C and another similar trend of weight loss after 400 °C. As mentioned above, the initial weight loss can be attributed to the release of physical adsorbed water molecules on the catalyst surface. After that, the oxygen vacancies can be re-filled with oxygen under high temperature, leading to a gentle weight loss of nanoplates and nanobelts. The weight loss after reoxidation was due to the desorption of chemisorption waters. TGA differential spectra of the nanosized samples with bulk Co_3O_4 are shown in Fig. 7(b). An increasing D-value (differential of residual mass between nanosized samples and bulk sample) has been presented after 200 °C, corresponding to the gentle weight loss stage in TGA curves. Then, D-value tends to a constant after 400 °C, indicating the final similar weight loss in TGA curves. From the D-value data, the amount of refilled oxygen can be obtained, which are directly related to the oxygen vacancies concentration. The D-value of Co_3O_4 nanobelts, nanoplates and nanosheets are 0.51%, 0.27% and 0.036%, respectively, indicating the oxygen vacancies concentration (the atom fraction of oxygen vacancies in total oxygen atoms) are 1.93%, 1.02% and 0.14%, respectively.

Figure 7. (a) TGA curve of different Co_3O_4 samples (b) The TGA differential spectra of nanoplates, nanobelts and nanosheets with bulk Co_3O_4.

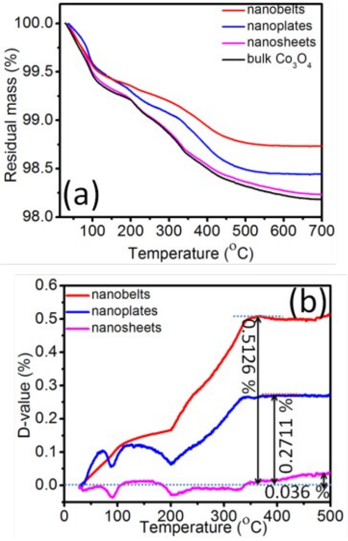

3.6 Thermal redox behavior of catalysts

The reducibility of different Co_3O_4 catalysts were studied by H_2-TPR technique (Fig. 8 a). The TPR profile presented two well-resolved reduction peaks, corresponding to the reduction of Co^{3+} to Co^{2+} (low-temperature peak) and Co^{2+} to Co^0 (high-temperature peak), respectively. Compared with the Co_3O_4 nanosheets, the reduction peaks of the nanoplates and the nanobelts showed remarkable shift to lower temperature, which could be attributed to the surface oxygen vacancies.[59] Surface oxygen vacancies promoted the reducibility of catalyst, facilitated the Co^{3+}/Co^{2+} redox and oxygen mobility. The synergistic effects between Co^{3+}/Co^{2+} and O/Vo redox speed up the oxygen transfer during HCHO oxidation process. As illustrated in Fig. 9, the Co^{2+} may initially interact with oxygen and then is oxidized into Co^{3+}. With the participation of oxygen vacancies, the activated oxygen is continuously transferred to HCHO, making HCHO oxidation happens. As known, high oxygen mobility will promote the catalytic oxidation activity.[21] Consequently, the reducibility shows a good accordance with their catalytic activity. The ratio of Co^{3+}/Co^{2+} can be obtained from the proportion of their reduction peak area. The small difference among three samples agreed with the XPS results which were shown in Table 1.

To further investigate the nature of adsorbed and activated oxygen species that will be involved in the formaldehyde oxidation reactions[29], O_2-TPD experiments were carried out as shown in Fig. 8b. According to the literatures[27, 39], the desorption peak at temperature about 200°C can be ascribed to molecular adsorption oxygen O- 2, and the desorption peak at temperature around 340°C belongs to the surface chemical adsorption oxygen O^-. These surface reactive oxygen species (ROS) are known to promote the catalytic oxidation reactivity.[6, 30] The desorption peak at temperature higher than 700°C belongs to the release of bulk phase lattice oxygen. Compared with the nanosheets, the nanoplates and the nanobelts presented obvious shifts of O_2 desorption peaks to lower temperature and higher intensities of desorption peaks. This phenomenon can be ascribed to the presence of surface oxygen vacancies. Their relative concentrations can be obtained by the desorption peak area.[21] Because O_2 activation played an important role in catalytic oxidation reactions, the facile supply and replenish of reactive oxygen species (ROS) probably lead to an outstanding catalytic performance for HCHO oxidation.

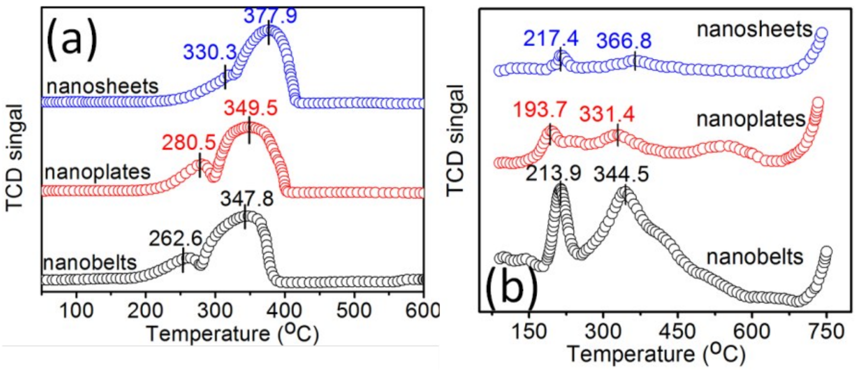

Figure 8. H_2-TPR and O_2-TPD profiles of Co_3O_4 nanobelts, nanoplates and nanosheets.

3.7 Mechanism discussion

Based on the above results, it is concluded that the catalytic performances of formaldehyde oxidation over Co_3O_4 catalysts are surface oxygen vacancies mediated. Catalytic activity shows a direct relationship with the concentration of surface oxygen vacancies. To further confirm the important role of surface oxygen vacancies played in this process, all the three samples were heat treated at 400 °C for 3 hours in air, according to the TGA results, to refill the oxygen vacancies, and then their catalytic formaldehyde oxidation activities at room temperature were checked. It is interesting to find out that all the catalysts lost their catalytic activities after annealing, which demonstrated the essential role of surface oxygen vacancies played in the catalytic formaldehyde oxidation reaction forcefully.

Accordingly, formaldehyde catalytic oxidation over Co_3O_4 catalyst with surface oxygen vacancies is schematically exhibited in Fig. 9. The synergistic effect between Co^{3+}/Co^{2+} and O/Vo redox greatly accelerates the active oxygen transfer. Moreover, the surface oxygen vacancies are favorable to reduce the chemisorption energy of oxygen molecules, and the surface chemisorbed O_2 can accept delocalized electrons from surface oxygen vacancies, be transformed into reactive oxygen species (ROS).[39, 54] Surface oxygen vacancies could also effectively bind reactants and assist in their reactions.[33, 45, 60] Thus, when Co_3O_4 with surface oxygen vacancies are exposed to formaldehyde atmosphere, the HCHO molecules are adsorbed on the surface of catalyst. Surface oxygen vacancies facilitate the activation of oxygen molecules and the easy replenishment of ROS. Then HCHO molecules can be oxidized into formate species rapidly, and finally mineralized into CO_2 and H_2O by reacting with ROS.

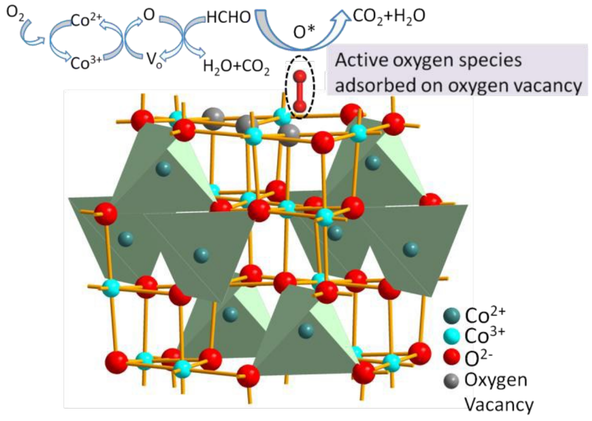

Figure 9. Schematic illustration of HCHO oxidation over Co_3O_4 with surface oxygen vacancies.

Conclusions

In summary, three kinds of Co_3O_4 catalysts with different concentration of surface oxygen vacancies were synthesized and their catalytic performances of HCHO oxidation at room temperature were evaluated. XPS, Raman spectra and TGA data confirmed the existence of surface oxygen vacancies. H_2-TPR and O_2-TPD results reveal the essential role of surface oxygen vacancies played in catalytic oxidation of formaldehyde, which are reflected by the improved mobility of oxygen and facile formation of reactive oxygen species (ROS). Consequently, catalytic activity shows a direct relationship with the concentration of surface oxygen vacancies. This study not only provides insights into the effect of surface oxygen vacancies on the catalytic oxidation of formaldehyde, but also provides a possibility for developing high performance catalysts through surface-modification.

Acknowledgements

We acknowledge financial support from the National Basic Research Program of China (2013CB933200) and the National Natural Science Foundation of China (51272269, 51272303, and 51472260).

Notes and references

1. T. Salthammer, S. Mentese and R. Marutzky, *Chem. Rev.*, 2010, **110**, 2536-2572.
2. L. Nie, A. Meng, J. Yu and M. Jaroniec, *Sci. Rep.*, 2013, **3**, 3215.
3. X. Tang, J. Chen, X. Huang, Y. Xu and W. Shen, *Appl. Catal. B: Environ.*, 2008, **81**, 115-121.
4. H. B. Huang and D. Y. C. Leung, *J. Catal.*, 2011, **280**, 60-67.
5. H. Huang and D. Y. C. Leung, *ACS Catal.*, 2011, **1**, 348-354.
6. Q. Xu, W. Lei, X. Li, X. Qi, J. Yu, G. Liu, J. Wang and P. Zhang, *Environ. Sci. Technol.*, 2014, **48**, 9702-9708.
7. C. Ma, D. Wang, W. Xue, B. Dou, H. Wang and Z. Hao, *Environ. Sci. Technol.*, 2011, **45**, 3628-3634.
8. Z. Xu, J. Yu and M. Jaroniec, *Appl. Catal. B: Environ.*, 2015, **163**, 306-312.
9. B.-b. Chen, X.-b. Zhu, M. Crocker, Y. Wang and C. Shi, *Appl. Catal. B: Environ.*, 2014, **154**, 73-81.
10. Z. Huang, X. Gu, Q. Cao, P. Hu, J. Hao, J. Li and X. Tang, *Angew. Chem. Int. Ed.*, 2012, **51**, 4198-4203.
11. J. Quiroz Torres, S. Royer, J. P. Bellat, J. M. Giraudon and J. F. Lamonier, *ChemSusChem*, 2013, **6**, 578-592.
12. Y. Xia, H. Dai, L. Zhang, J. Deng, H. He and C. T. Au, *Appl. Catal. B: Environ.*, 2010, **100**, 229-237.
13. L. Bai, F. Wyrwalski, J.-F. Lamonier, A. Y. Khodakov, E. Monflier and A. Ponchel, *Appl. Catal. B: Environ.*, 2013, **138-139**, 381-390.
14. D. Su, S. Dou and G. Wang, *Sci. Rep.*, 2014, **4**, 5767.
15. G. Tong, J. Guan and Q. Zhang, *Adv. Funct. Mater.*, 2013, **23**, 2406-2414.
16. J. Y. Kim, N.-J. Choi, H. J. Park, J. Kim, D.-S. Lee and H. Song, *J. Phys. Chem. C*,2014, **118**, 25994-26002.
17. X. Xie, Y. Li, Z. Q. Liu, M. Haruta and W. Shen, *Nature*, 2009, **458**, 746-749.
18. C. Y. Ma, Z. Mu, J. J. Li, Y. G. Jin, J. Cheng, G. Q. Lu, Z. P. Hao and S. Z. Qiao, *J.Am. Chem. Soc.*, 2010, **132**, 2608-2613.
19. L. Hu, Q. Peng and Y. Li, *J. Am. Chem. Soc.*, 2008, **130**, 16136-16137.
20. H. Wang, C. Chen, Y. Zhang, L. Peng, S. Ma, T. Yang, H. Guo, Z. Zhang, D. S. Su and J. Zhang, *Nat. Commun.*, 2015, **6**, 7181.
21. Y. Lou, J. Ma, X. Cao, L. Wang, Q. Dai, Z. Zhao, Y. Cai, W. Zhan, Y. Guo, P. Hu, G. Lu and Y. Guo, *ACS Catal.*, 2014, **4**, 4143-4152.
22. Y. Yu, T. Takei, H. Ohashi, H. He, X. Zhang and M. Haruta, *J. Catal.*, 2009, **267**, 121-128.
23. W. J. Xue, Y. F. Wang, P. Li, Z.-T. Liu, Z. P. Hao and C. Y. Ma, *Catal. Commun.*, 2011, **12**, 1265-1268.
24. T. E. Davies, T. Garcia, B. Solsona and S. H. Taylor, *Chem. Commun.*, 2006, **32**, 3417-3419.
25. J. Deng, L. Zhang, H. Dai, Y. Xia, H. Jiang, H. Zhang and H. He, *J. Phys. Chem. C*, 2010, **114**, 2694-2700.
26. B. Bai and J. Li, *ACS Catal.*, 2014, **4**, 2753-2762.
27. B. Bai, H. Arandiyan and J. Li, *Appl. Catal. B: Environ.*, 2013, **142**, 677-683.
28. B. Solsona, T. E. Davies, T. Garcia, I. Vazquez, A. Dejoz and S. H. Taylor, *Appl. Catal. B: Environ.*, 2008, **84**, 176-184.
29. B. de Rivas, R. Lopez-Fonseca, C. Jimenez-Gonzalez and J. I. Gutierrez-Ortiz, *J. Catal.*, 2011, **281**, 88-97.
30. L. F. Liotta, H. Wu, G. Pantaleo and A. M. Venezia, *Catal. Sci. Technol.*, 2013, **3**, 3085-3102.
31. G. Kimmel and N. Petrik, *Phys. Rev. Lett.*, 2008, **100**.
32. P. Scheiber, A. Riss, M. Schmid, P. Varga and U. Diebold, *Phys. Rev. Lett.*, 2010, **105**.
33. E. W. McFarland and H. Metiu, *Chem. Rev.*, 2013, **113**, 4391-4427.
34. J. Yu, X. Li, Z. Xu and W. Xiao, *Environ. Sci. Technol.*, 2013, **47**, 9928-9933.
35. L. Kong, Z. Jiang, C. Wang, F. Wan, Y. Li, L. Wu, J. F. Zhi, X. Zhang, S. Chen and Y. Liu, *ACS Appl. Mater. Interfaces*, 2015, **7**, 7752-7758.
36. Y. Wang, Z. Zhong, Y. Chen, C. T. Ng and J. Lin, *Nano Res.*, 2011, **4**, 695-704.
37. D. Su, S. Dou and G. Wang, *Nano Res.*, 2014, **7**, 794-803.
38. Y. Wang, C. Zhang, Y. Yu, R. Yue and H. He, *Catal. Today*, 2015, **242**, 294-299.
39. Q. Liu, L.-C. Wang, M. Chen, Y. Cao, H.-Y. He and K.-N. Fan, *J. Catal.*, 2009, **263**, 104-113.
40. Y. Lou, L. Wang, Z. Zhao, Y. Zhang, Z. Zhang, G. Lu, Y. Guo and Y. Guo, *Appl. Catal. B: Environ.*, 2014, **146**, 43-49.
41. C. Zhang, F. Liu, Y. Zhai, H. Ariga, N. Yi, Y. Liu, K. Asakura, M. Flytzani-Stephanopoulos and H. He, *Angew. Chem. Int. Ed.*, 2012, **51**, 9628-9632.
42. P. Hu, Z. Amghouz, Z. Huang, F. Xu, Y. Chen and X. Tang, *Environ. Sci. Technol.*, 2015, **49**, 2384-2390.
43. B.-T. Liu, C.-H. Hsieh, W.-H. Wang, C.-C. Huang and C.-J. Huang, *Chem. Eng. J.*,2013, **232**, 434-441.
44. Y. Wang, X. Zhu, M. Crocker, B. Chen and C. Shi, *Appl. Catal. B: Environ.*, 2014, **160-161**, 542-551.
45. S. J. Park, I. Bae, I.-S. Nam, B. K. Cho, S. M. Jung and J.-H. Lee, *Chem.Eng.J.*, 2012, **195-196**, 392-402.
46. C. B. Zhang, H. He and K. Tanaka, *Appl. Catal. B: Environ.*, 2006, **65**, 37-43.
47. H. F. Wang, R. Kavanagh, Y. L. Guo, Y. Guo, G. Z. Lu and P. Hu, *Angew. Chem. Int. Ed.*, 2012, **51**, 6657-6661.
48. H. Huang, X. Ye, H. Huang, L. Zhang and D. Y. C. Leung, *Chem. Eng. J.*, 2013, **230**, 73-79.
49. D. W. Kwon, P. W. Seo, G. J. Kim and S. C. Hong, *Appl. Catal. B: Environ.*, 2015, **163**, 436-443.
50. T. W. Kim, M. A. Woo, M. Regis and K.-S. Choi, *J. Phys. Chem. Lett.*, 2014, **5**, 2370-2374.
51. Y. Wang, T. Zhou, K. Jiang, P. Da, Z. Peng, J. Tang, B. Kong, W.-B. Cai, Z. Yang and G. Zheng, *Adv. Energy Mater.*, 2014, **4**, 1400696.
52. D. A. Tompsett, S. C. Parker and M. S. Islam, *J. Am. Chem. Soc.*, 2014, **136**, 1418-1426.
53. K. Zhao, L. Zhang, J. Wang, Q. Li, W. He and J. J. Yin, *J. Am. Chem. Soc.*, 2013, **135**, 15750-15753.
54. L. Zeng, W. Song, M. Li, D. Zeng and C. Xie, *Appl. Catal. B: Environ.*, 2014, **147**,490-498.
55. S. Deng, X. Xiao, X. Xing, J. Wu, W. Wen and Y. Wang, *J. Mol. Catal. A: Chem.*, 2015, **398**, 79-85.
56. L. Li, J. Yan, T. Wang, Z. J. Zhao, J. Zhang, J. Gong and N. Guan, *Nat. Commun.*, 2015, **6**, 5881.
57. A. Naldoni, M. Allieta, S. Santangelo, M. Marelli, F. Fabbri, S. Cappelli, C. L. Bianchi, R. Psaro and V. Dal Santo, *J. Am. Chem. Soc.*, 2012, **134**, 7600-7603.
58. H. Tan, Z. Zhao, W. B. Zhu, E. N. Coker, B. Li, M. Zheng, W. Yu, H. Fan and Z. Sun, *ACS Appl. Mater. Interfaces*, 2014, **6**, 19184-19190.

59. J.-b. Li, Z.-q. Jiang, K. Qian and W.-x. Huang, *Chinese J. Chem. Phys.*, 2012, **25**, 103-109.
60. J. M. López, A. L. Gilbank, T. García, B. Solsona, S. Agouram and L. Torrente-Murciano, *Appl. Catal. B: Environ.*, 2015, **174-175**, 403-412.

Table of Contents:

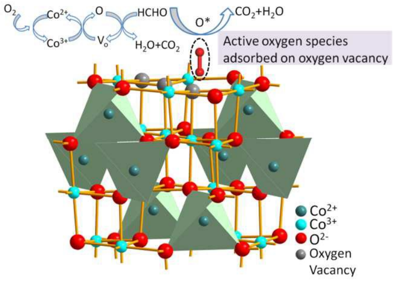

This study reveals the essential role of surface oxygen vacancies played in catalytic oxidation reactions, and complements the common viewpoint of Co^{3+} is the major activity species in the Co_3O_4-based systems.